

# Angle-resolving time-of-flight electron spectrometer for near-threshold precision measurements of differential cross sections of electron-impact excitation of atoms and molecules

M. Lange,<sup>a)</sup> J. Matsumoto,<sup>b)</sup> A. Setiawan, R. Panajotović,<sup>c)</sup> J. Harrison, J. C. A. Lower, D. S. Newman, S. Mondal, and S. J. Buckman  
*Centre for Antimatter-Matter Studies, Research School of Physical Sciences and Engineering,  
 The Australian National University, Canberra 0200 ACT, Australia*

(Received 25 December 2007; accepted 31 March 2008; published online 28 April 2008)

This article presents a new type of low-energy crossed-beam electron spectrometer for measuring angular differential cross sections of electron-impact excitation of atomic and molecular targets. Designed for investigations at energies close to excitation thresholds, the spectrometer combines a pulsed electron beam with the time-of-flight technique to distinguish between scattering channels. A large-area, position-sensitive detector is used to offset the low average scattering rate resulting from the pulsing duty cycle, without sacrificing angular resolution. A total energy resolution better than 150 meV (full width at half maximum) at scattered energies of 0.5–3 eV is achieved by monochromating the electron beam prior to pulsing it. The results of a precision measurement of the differential cross section for electron-impact excitation of helium, at an energy of 22 eV, are used to assess the sensitivity and resolution of the spectrometer. © 2008 American Institute of Physics. [DOI: 10.1063/1.2912824]

## I. INTRODUCTION

For electron-atom(molecule) scattering, the energy region within a few electron volts of the electronic excitation thresholds, is an interesting one for both experiment and theory. This region is a challenge experimentally particularly with regard to establishing the absolute magnitude of the measured scattering cross sections. For angular differential scattering measurements, the most commonly used approach has been to measure the flux of inelastically scattered electrons relative to that for the elastic scattering intensity at the same incident energy and scattering angle. For most atoms and molecules that are gases at room temperature, the elastic scattering cross sections are now reasonably well established through the use of the relative flow technique (see, e.g., Ref. 1). If the transmission of the energy analyzing device is known, the inelastic scattering cross section can be readily determined from the ratio of scattered electron intensities. The main experimental issue that has to be resolved when using this approach is usually the determination of the transmission of the energy analyzing device (e.g., a hemispherical analyzer) as a function of the scattered electron energy.

At high incident energies ( $>100$  eV), it is common, and relatively sound practice for the analyzer transmission to be assumed to be constant, even for relatively tightly bound systems such as the rare gases where the excitation energies

are in excess of 10 eV. However, as the incident energy approaches the excitation threshold, the ratio of the scattered electron energies for elastic and inelastic processes can be significant, and some strategy must be adopted for measuring, or estimating, the analyzer transmission function in order to obtain accurate absolute cross sections for the inelastic events. A number of recent approaches<sup>2,3</sup> have therefore involved careful measurements of the analyzer transmission as a function of energy in order to obtain absolute cross sections.

The strategy that is used in the present work is to employ time-of-flight (ToF) energy analysis in a field-free environment in order to overcome the energy dependence issues of the scattered electron analyzer. Only a few low-energy ToF electron spectrometers have been reported in the literature over the past two decades, for example in Refs. 4 and 5, with the former one being the more recent and the one for which a variety of measurements has been reported. For solid targets, Ref. 6 also reported the use of the ToF method to resolve low-energy scattering channels.

Our apparatus differs from these in several important points: Firstly, the spectrometers in Refs. 4 and 5 are limited in energy resolution by the large energy spread (0.5–0.6 eV) of their unmonochromatized electron beams, while our pulsed electron gun reaches an energy spread below 150 meV by the use of a hemispherical monochromator. Secondly, both of the above crossed-beam spectrometers can only probe the electron-target interaction at one particular scattering angle ( $90^\circ$  for Ref. 4 and  $0^\circ$  for Ref. 5) because their electron guns are fixed in position relative to the detector system, while our gun can be rotated about the target beam to access scattering angles of  $45^\circ$ – $130^\circ$ . Finally, we use a large position-sensitive detector to increase electron detec-

<sup>a)</sup>Present address: Max-Planck-Institut für Kernphysik, Postfach 10 39 80, 69029 Heidelberg, Germany. Electronic mail: michael.lange@mpi-hd.mpg.de.

<sup>b)</sup>Present address: Department of Chemistry, Tokyo Metropolitan University, 1-1, Minami-ohsawa, Hachioji, Tokyo 192-0397, Japan.

<sup>c)</sup>Present address: Department of Physics and Astronomy, Faculty of Science, The Open University, Milton Keynes MK7 6AA, United Kingdom.

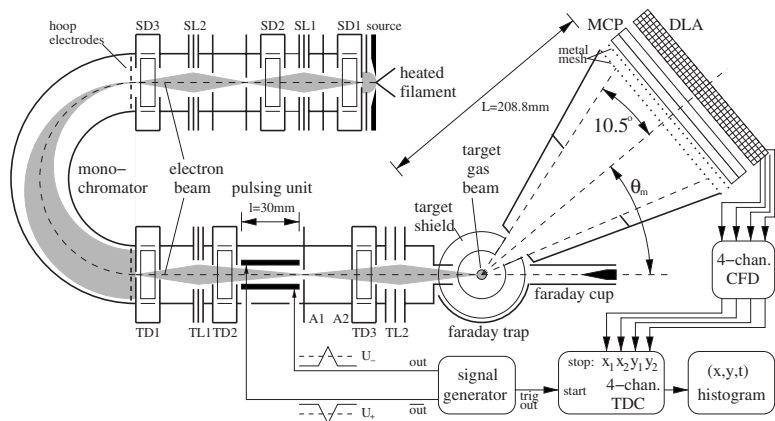


FIG. 1. Schematic drawing of the spectrometer as seen from above (not to scale). As explained in the text, the electron gun is shown rotated by  $90^\circ$  about the axis of the electron beam in the target optics. Abbreviations used for labeling optics: S is the source optics, T is the target optics, L is the electrostatic lenses, D is the electrostatic deflectors, A is the important apertures.

tion rates while maintaining high levels of angular resolution. A large fraction of this paper is therefore devoted to a detailed description of our spectrometer, especially the pulsed electron gun. Following this, we describe the data acquisition (DAQ) and analysis procedure using a recent benchmark measurement of the differential cross section for electron-impact excitation of helium as an example.

## II. SPECTROMETER

A schematic overview of our crossed-beam ToF spectrometer is shown in Fig. 1. It consists of a pulsed electron gun (to the left of the drawing) that can be rotated about the axis of the target gas beam (at the center of the drawing), and a time- and position-sensitive detector system mounted at the base of a field-free drift tube of conical shape (on the right). The overlap of the target gas and pulsed-electron beam defines the interaction volume. The start of each beam pulse serves as the time reference for measuring the ToF of the electrons scattered by the continuous target beam. The present small electron beam intensity imposed by the low duty cycle of the pulsing/measuring process is offset by the use of a detector with a large acceptance area. Its position sensitivity enables precise measurement of the scattering angle of each detected electron, so that an angular resolution comparable to most other spectrometers is maintained. More importantly, the ToF method enables simultaneous measurement of all energy-loss processes from zero to maximum energy loss, thereby measuring all scattering channels (including the elastic one) concurrently. This, and the absence of electrostatic optical elements in the detection branch of the spectrometer makes for an almost energy-independent transmission of the analyzer, so that no corrections for apparatus functions have to be applied to the measured scattering intensities before obtaining the inelastic-to-elastic ratio of the differential cross section.

### A. Experiment chamber

The electron gun, target beam, and detector system are located within a cylindrical vacuum chamber pumped by a combination of a  $500 \text{ l s}^{-1}$  turbomolecular pump backed with a  $20 \text{ m}^3 \text{ h}^{-1}$  rotary vane pump. After light baking at  $80^\circ \text{C}$ , a base pressure of  $5 \times 10^{-8}$  mbar is achieved. Magnetic materials have been avoided as far as possible in the construction of the chamber, its support frame and the spectrometer com-

ponents, with most metal parts being made of either nonmagnetic stainless steel or aluminum. With a few noted exceptions all metal parts exposed to the electron beam are either made from or lined with molybdenum, to maintain a uniform and well-defined surface potential, and to reduce secondary electron emission. Throughout the chamber, insulators of structural importance are made from either ceramic, fused silica or ruby, while polytetrafluoroethylene (PTFE) or Kapton insulation has been used for flexible electrical wiring.

To minimize disturbance of the low-energy electrons by the earth's magnetic field, the vacuum chamber is located inside a closed, rectangular box of  $\mu$ -metal shielding. A second layer of shielding, in the shape of a vertical cylinder with an open base is mounted inside the vacuum chamber. The remaining magnetic field was measured to be  $<0.3 \mu\text{T}$  at the interaction volume. It changes by less than  $\pm 0.1 \mu\text{T}$  when the electron gun is rotated on its turntable. The stationary fraction of the field is compensated to  $<0.02 \mu\text{T}$  at the center of the interaction volume, by running an electric current through three orthogonal pairs of rectangular coils located between the outer shielding box and the vacuum chamber. Although the coils of each pair are placed at a distance somewhat greater than for an exact Helmholtz geometry, this arrangement still provides good compensation even away from the collision center, while allowing easier access to the spectrometer.

### B. Electron gun

The electron gun consists of three sections: An electron source with attached electrostatic optics ("source stack"), which is mounted to a  $180^\circ$  hemispherical monochromator, and the electrostatic optics (including a beam pulsing unit) leading to the target gas beam ("target stack"). Since, in reality, the source stack is located above the target stack, the electron gun in Fig. 1 is shown rotated by  $90^\circ$  about the beam axis of the target stack for ease of viewing. The only exception to this are the deflector plates of the pulsing unit, which are shown in their true orientation with respect to the rest of the apparatus.

#### 1. Production of the continuous electron beam

A directly heated hairpin filament, made from thoriated tungsten is used to produce a continuous electron beam with an energy spread of  $0.5\text{--}0.6 \text{ eV}$ . A microstructured field-

emitting cathode has also been investigated<sup>7</sup> as an alternative source of electrons, because the operation at room temperature suggested a smaller energy spread in the emitted beam. However, our measurements revealed an energy spread of 1 eV for this source, so that the tungsten filament was kept for all measurements presented in this paper. The filament is located in the opening of a repeller shield of the Pierce geometry<sup>8</sup> which is kept at a negative voltage with respect to the filament, to partially compensate radial expansion of the beam caused by space charge. The electrons are accelerated to 80 eV by a ring anode whose aperture (1 mm diameter) serves as the primary object for the following system of electrostatic optics. Despite their larger aberrations, aperture lenses have been chosen instead of cylindrical lenses throughout the electron gun because they are generally more compact in the axial direction: two electrostatic lenses SL1 and SL2 project an unmagnified image of the anode hole onto the entrance of the electrostatic monochromator, with the electron beam being collimated by additional apertures placed in the object plane and in the primary focal plane of each electrostatic lens. The lenses are also used to decelerate the electrons from the anode energy, in a first step to an intermediate energy of 20 eV, and then to the pass energy of the monochromator. In addition, three lateral electrostatic deflector sets SD1-3 are used to control the position and inclination of the electron beam with respect to the optical axis of the gun elements.

The collimated and retarded beam is passed through a monochromator of 180° hemispherical type with a mean radius of 39.5 mm and six fringe-field correcting hoop electrodes to correct field distortions caused by the transition from cylindrical to spherical geometry. The image of the collimating pupil before SL2 is used as a virtual entrance aperture to the monochromator, while a physical aperture of 0.9 mm diameter is placed at the exit. The common practice of using another virtual aperture in the latter position cannot be adopted here because the pulsing unit (immediately located after the first lens downstream from the monochromator) requires an energy-selected beam with a well-defined envelope, and there is not enough space for additional optical elements. Both hemisphere shells are made of molybdenum, and the outer one is kept at 100 °C at all times by a coaxial noninductive electric heater, to prevent contamination of this large surface located close to the beam. However, a buildup of some electrically insulating deposit has been observed on the hoop electrodes as well as the support plate (all stainless steel). This is removed every few months with a clean dry piece of scrubbing pad, to avoid the complete dismantling of the electron gun for a lengthy wet cleaning process of the monochromator.

## 2. Beam pulsing unit

Before reaching the target, the monochromatized beam is chopped into short pulses, to provide a time reference for the ToF measurement. The duration of these pulses should be shorter than 10 ns [full width at half maximum (FWHM)] for good resolution of scattering channels in the measured ToF spectra. This is achieved by sweeping the electron beam across the chopping aperture A1 in Fig. 1, by operating two

deflector plates with fast voltage transients. The deflection plates are made from titanium, and have a length of 30 mm and a 7 mm gap. Since over 99% of the continuous beam current is being dumped at A1, this part is made of molybdenum. Because of the difficulty of manufacturing from this material, it does not have the skimmer shape which is most favorable for minimizing beam halo, but consists of a 0.15 mm thin plate with a 1.5 mm hole. Further apertures have been mounted downstream of the pulsing unit to strip any halo arising from A1.

Several precautions have been taken to minimize the influence of the pulsing process on the electron beam energy spread: first, since all detrimental effects on energy spread should generally increase with deflection voltage, the monochromator exit is imaged by lens TL1 onto aperture A1, where it has a waist of 1.5 mm diameter. This allows the use of a much smaller aperture and consequently a smaller deflection voltage than for a divergent or even a parallel beam. Second, the deflector plates are mounted such that the electrons are deflected in the horizontal rather than the vertical plane (see Fig. 1). This way, the deflection of the beam is always perpendicular to the direction of largest energy dispersion of the monochromator, hence, any of this dispersion which may be preserved at the image of the monochromator exit created at A1 will not cause a sweep of the mean energy of the transmitted electrons as the beam is scanned over the aperture. Finally, we apply the so-called toggle method which has also been used for the pulsed electron guns in Refs. 4 and 6, and which is described in more detail in Ref. 9: two voltage transients of symmetric triangular shape and with opposite polarity are generated by a Hewlett-Packard 8082A pulse generator, with amplitudes around 1 V and with common base lengths  $\tau$  matched to the drift time of the electrons through the pulsing unit ( $\tau=16$  ns at a transition energy of  $eU_{\text{PU}}=10$  eV, where  $U_{\text{PU}}$  is the potential at the central plane of the pulsing-unit deflector gap). The transients are superimposed on constant voltages in a resistor network. Their inversion symmetry with respect to one another ensures that  $U_{\text{PU}}$  remains constant at all times. The time dependence of the resulting voltages  $U_{-}(t)$  and  $U_{+}(t)$  is shown as the two schematic oscillograph traces next to the signal transmission cables in Fig. 1, with  $U_{\text{PU}}$  indicated by the dashed line. In this arrangement, the beam is deflected to the side of the aperture hole most of the time. Only for those electrons which enter the deflector gap at the time when a voltage pulse starts, will the displacement and velocity gain imparted in the transversal direction be completely canceled at the exit of the pulsing unit. Electrons entering the pulsing unit at an earlier or later time than when the transient is first applied are displaced in the transversal direction and will therefore not be transmitted through A1. Most importantly, those electrons which are transmitted by the pulsing unit will experience identical static fringing fields when entering and exiting the unit, resulting in a cancellation of longitudinal momentum transfers from the fringe fields, thereby suppressing a possible source of energy broadening. More detailed modeling shows that a second aperture A2 is needed to discriminate against electrons which enter the pulsing unit at a time  $\approx \tau/2$  before a pulse starts, and which exhibit zero dis-

placement at A1 but acquire a certain transversal velocity (and energy) and hence a nonzero beam angle. For those electrons transmitted through both A1 and A2, the maximum possible beam angle translates to a gain in energy which is negligible compared to the energy spread even of the unpulsed beam. Therefore, both the mean and the width of the electron energy distribution should be largely conserved in this particular pulsing scheme, which is its main advantage compared, e.g., to a beam sweep over an aperture effected by the shoulder of a rectangular signal. As pointed out in Ref. 4, it has the additional advantage that the base length of the triangular signal may be somewhat longer than the required electron pulse duration, which helps reduce the maximum frequency that must be properly transmitted through cables and vacuum feedthroughs.

The fast deflection voltages are transmitted to the deflector plates using 50  $\Omega$  coaxial cable and vacuum feedthroughs with a matched impedance and SMA plugs on both the air and vacuum sides. Although they contain magnetic materials, they are far enough away from the interaction volume (and inside the  $\mu$ -metal shielding box) to be of no concern. Standard flexible RG58 cable is used for guiding the pulsing voltages, even inside the vacuum chamber, because many ultrahigh vacuum versions of this type are very rigid (thus interfering with the turntable movement) or are not sufficiently nonmagnetic. However, the outer insulation has been stripped from the cables and replaced with short rings of PTFE heat shrink tube every 10 cm, to reduce outgassing and to increase pumping speed for the gas volume otherwise trapped within the shielding braids, while keeping those braids in place and tight around the core of the cable when the electron gun is moved. Alternating currents are terminated at the end of each cable by a 50  $\Omega$  resistor and a 100 pF capacitor connected in series and mounted in the vacuum chamber, only a few centimeters away from the corresponding pulsing plate. This reduces reflection of the transients at the end of the cables and allows superposition of the constant voltages while drawing negligible direct current.

### C. Scattering region

Before it is directed at the target gas beam, the pulsed electron beam is accelerated to the desired projectile energy  $E$  by lens TL2. This means that the pulsing occurs at a fixed energy, eliminating the need to adjust the duration and slope of the pulsing transient every time the projectile energy is changed. The lens also defines the electron beam waist at the beam crossing and thus the collision volume. The exit nozzle of the electron gun has been shaped as a narrow cylinder to help eliminate any beam halo which might arise from scattering at the fringes of the pulsing apertures. Simulations of the electron gun with the SIMION software<sup>10</sup> show that the diameter of the electron beam at the location of the target varies between 1 mm at  $E=20$  eV and 1.5 mm at  $E=5$  eV, while the spreads in beam angle are  $\pm 2^\circ$  and  $\pm 3.5^\circ$ , respectively.

The electrons cross a beam of the target gas, which effuses from a single capillary (stainless steel) of 1 mm inner diameter. Gas is supplied from a large, low-pressure tank to eliminate the pressure fluctuations associated with the use of

a high-pressure gas bottle and a pressure regulator. We therefore obtain a very constant gas flow which can be finely adjusted by a needle valve. The usual capillary drive pressure is  $\approx 1$  mbar, which corresponds to a stationary background pressure of  $< 5 \times 10^{-6}$  mbar in the spectrometer vacuum chamber. Under these conditions, the diameter of the gas beam is estimated to be  $\approx 1.5$  mm at the beam crossing. However, for the present spectrometer geometry which incorporates a relatively long drift tube and a large position-sensitive detector, energy-loss- and angular resolution are relatively insensitive to the size of the collision volume.

As indicated in Fig. 1, the beam crossing is located at the center of a target enclosure made from four titanium discs or rings stacked vertically at a spacing of 5 mm. The two middle rings are made from 0.125 mm thickness shim and have a segment cut out near the entrance to the detector to avoid small-angle scattering of electrons from solid surfaces into the drift cone. The stack is terminated at the top by a similar ring that has no cutout but the central hole covered with mesh. At the bottom is a thicker plate that holds the gas capillary. The whole enclosure is at the same potential as the exit nozzle of the electron gun. This arrangement ensures that the enclosure is more than 90% transparent for electrons scattered close to the horizontal plane, thus minimizing the area of solid surfaces from which electrons can be reflected back into the detector. At the same time, the very good attenuation of external electric fields enables further reduction of the amount of electrons reflected from spectrometer parts outside of the target region to be achieved by introducing a collector plate wrapping around the target in a semicircle. This plate is biased at +40 V above the potential of the target enclosure to act as a Faraday trap for scattered electrons. For dumping the primary beam, a Faraday cup is also mounted opposite of the electron gun. We have verified that the target region is adequately shielded against the voltages of both the trap and the cup, by comparing differential cross sections measured both with the collector voltages on and off. While no significant difference was found in the angular dependence of the cross section, the comparison showed that background from electrons scattered by other sources than the target beam was reduced at least by a factor of 2 (see below for details).

### D. Detector system

Electrons scattered into the direction of the detector enter a hollow cone made of aluminium and lined with titanium shim on the inside. Two titanium apertures—one at the tip of the cone and one halfway down its length—prevent close contact between scattered electrons and the inner surface of the cone. The cone is kept on the same potential as the exit nozzle of the gun and the target enclosure, so that the electrons drift through a field-free region over a length of  $L=208.8$  mm, measured from the crossing of the electron and target beam axes to the far end of the cone. There, the field-free region is terminated by a layer of high-transparency ( $>90\%$ ) copper mesh. Electrons transmitted through this mesh are postaccelerated to  $\approx 300$  eV, by voltages applied to a second mesh (molybdenum) and to the

front of the detector, which makes detection efficiency independent of the energy lost in the scattering event.

The detector system consists of a chevron stack of two micro-channel plates (MCPs) (Hamamatsu) of 80 mm diameter and a thickness of 1.5 mm each, which is mounted to an  $80 \times 80 \text{ mm}^2$  square wire-coil delay line anode (DLA) [RoentDek DLA80 (Ref. 11)]. The four signals picked up between the signal and the reference windings at the ends of each delay line—two signals for the horizontal ( $x$ ) and two for the vertical ( $y$ ) direction—are amplified and fed to four constant-fraction discriminators (CFDs) in a trigger unit (RoentDek DLA-TR6). The arrival times  $t_{x1}$ ,  $t_{x2}$ ,  $t_{y1}$ , and  $t_{y2}$  of all four DLA signals are measured by a four-channel time-to-digital converter (TDC) (RoentDek HM-1), relative to a common start signal which is taken from the HP signal generator that operates the beam pulsing unit. From the time differences  $t_{x1} - t_{x2}$  and  $t_{y1} - t_{y2}$ , the spatial coordinates ( $x, y$ ) of a scattered electron on the MCP front are inferred, while the sum  $t = (t_{x1} + t_{x2})/2$  is equal to the time of flight of the scattered electron, plus an unknown but constant delay arising from signal propagation along cables and processing times in the electronics. This delay is calculated during data analysis from the difference between the measured and the calculated flight time of elastically scattered electrons (see below). The distribution of scattered electrons in the ( $x, y, t$ ) space (detector coordinates) is measured by accumulating a three-dimensional histogram in a computer memory which is built into the TDC unit and which is read out regularly from a personal computer.

### III. MEASUREMENT OF THE SCATTERING ANGLE

Because the direction of the scattered electron momentum is preserved during the drift, the angle  $\theta_c$  enclosed between the electron momentum vector and the axis of the detector cone translates into a radial distance  $r = L \tan \theta_c$  of the electron at the base of the cone (in the plane of the MCP). Together with the known angle  $\theta_m$  (see Fig. 1) between the axes of the electron gun and the detector cone, the individual scattering angle  $\theta$  of each detected electron can be inferred from the detector coordinates  $x$  and  $y$ , which are measured with respect to the detector center.  $\theta_m$  can be adjusted between  $55^\circ$  and  $120^\circ$  by rotating the turntable on which the electron gun is mounted. Together with the large angular acceptance of the detector ( $|\theta_c| \leq 10.5^\circ$ ), a total range of scattering angles of  $\theta = 45^\circ - 130^\circ$  is accessible for cross-section measurements. The scattering angle can, in principle, be determined from the detector coordinates by the exact expression

$$\theta = \arctan \frac{\sqrt{(L \sin \theta_m + x \cos \theta_m)^2 + y^2}}{L \cos \theta_m - x \sin \theta_m}. \quad (1)$$

However, in our case, where the spectrometer accepts only a limited range of azimuthal angles around the electron beam axis, the approximation

$$\theta \approx \frac{x}{L} + \theta_m \quad (2)$$

deviates from the exact transformation by no more than  $\pm 0.75^\circ$ , much less than the angular spread of the electron beam and hence the experimental uncertainty of the measured scattering angle. The approximation has the advantage that  $\theta$  is now independent of  $y$ , which largely corresponds to the azimuthal angle of the scattered electron momentum around the electron beam axis. Since this angle holds no information about the scattering process, the acquired ( $x, y, t$ ) histograms are integrated over the  $y$  coordinate. Then, the above approximate transformation is applied and the data rebinned along the  $\theta$  coordinate to yield ten ToF spectra (“slices”), each covering a range of  $2^\circ$  centered about an integer scattering angle. Because the main experimental focus with this spectrometer is to measure inelastic scattering we directly compare particle counts from the elastic and inelastic channels at identical scattering angles and thus it is not necessary to normalize the slices according to the area of the detector integrated over. Of course, for a direct measurement of a single channel such a normalization to bin size would be necessary.

Compared to the typical width of the scattered electron flight time distribution (which is dominated by the temporal and energy spread of the pulsed beam and can amount to 10–50 ns, depending on the scattered electron energy), the intrinsic time resolution of the detector system of 266 ps, as well as the slight change in the length of the flight path with  $\theta_c$  have a relatively small effect on the energy resolution of the spectrometer. Similarly, the detector spatial resolution of 0.2 mm maps to an angular resolution of 1 mrad, which is negligible compared to the angular spread of the electron beam ( $\pm 2^\circ$ ). The intrinsic resolution of the detector system is therefore only of minor importance to the overall precision of the spectrometer and is therefore ignored from now on.

### IV. DATA ACQUISITION AND EXPERIMENT PROCEDURE

DAQ and control of most experimental parameters, such as setting the electron energy and median scattering angle and selecting the gas inlet (see below) is mostly automated by National Instruments LABVIEW running on a DAQ personal computer (PC). A noted exception to this are the electrostatic optics potentials, which are set manually. Every 15 min, the histogram memory of the HM1 unit is read out by a program supplied with the device. It is called from within the main LABVIEW routine so that the readout can be synchronized with other software or hardware actions. Each histogram is stored in a separate file on the PC, together with a time stamp and the 15 min averages of several apparatus parameters, such as the pressure reading of an ionization gauge installed to the main chamber (Granville-Phillips 274 gauge on 307 controller), the electron current measured by a picoammeter (Keithley 485) connected to the pulsing aperture A1, and the reading of an MKS Baratron gauge (model 722) exposed to the drive pressure of the target capillary and read out by a National Instruments 6025 DAQ computer card. Also, a history is kept by the computer of the voltages

of several electrodes of the electrostatic optics (e.g., target potential, hemisphere, and pulsing unit pass voltages). The median scattering angle is set by means of a rotating manipulator and a step motor, driven by a National Instruments 6601 timer/counter computer card.

A measurement of the inelastic-to-elastic differential cross-section (DCS) ratio over the whole accessible range of scattering angles is accomplished by successively moving the median scattering angle  $\theta_m$  in steps of  $10^\circ$  (corresponding to a shift of the image on the detector by half of its diameter) and accumulating data for several hours to days at each position. To eliminate the contribution to the accumulated  $(x, y, t)$  histograms from electrons which have been scattered toward the detector, either by parts of the spectrometer itself or by the dilute residual gas in the vacuum chamber, every second hour of an experiment is spent on a background measurement. There, the gas supply is redirected from the target to a capillary of similar dimensions, which is mounted far from the target enclosure and pointing away from it. While the resulting gas beam has no intersection with the electron beam, the pressure in the vacuum chamber remains largely the same as during the measurements with the target capillary, so that data obtained under these conditions can be used in a background subtraction. Before performing this background subtraction, the ToF spectra obtained in both “signal” and “background” mode are always normalized to the respective averages of chamber pressure and electron current, to account for possible long-term drifts or systematic differences between the modes of operation.

Before, and repeatedly during an experiment, DCS DAQ is paused, and the electron gun is switched to continuous beam mode for a calibration of the absolute beam energy: because the cathode is biased by a voltage to compensate work functions, etc., the electron beam usually has a small excess energy  $\Delta E$  above what is expected from the voltage applied to any particular electrostatic element, including the target cage and drift cone. This energy shift is determined from the total cross section for production of metastable excited target atoms by electron-impact (the excitation function), which is measured as a function of beam energy with a single channel electron multiplier placed in the gas beam above the target cage (not shown in Fig. 1). By comparing the known position of a feature in the excitation function to the voltage at which it is observed, the energy shift  $\Delta E$  is inferred. For the measurements on helium presented in this paper, we have used a negative ion resonance in the excitation function for metastable helium atoms,<sup>12</sup> which appears at an energy of 22.45 eV. The energy scale can thus be established with an experimental uncertainty of  $\pm 30$  meV.

Since this resonance has a small natural linewidth, the measured width is also an indicator for the energy spread of the unpulsed electron beam. From such measurements, we have repeatedly obtained energy spreads between 40 and 70 meV (FWHM) for an unpulsed beam, which is somewhat narrower than expected from the voltages applied to the beam monochromator. Similar measurements have also been performed with the pulsed beam, but they are less conclusive because the energy spread increases while the beam current is reduced to  $\approx 0.5\%$  of its value in continuous beam mode,

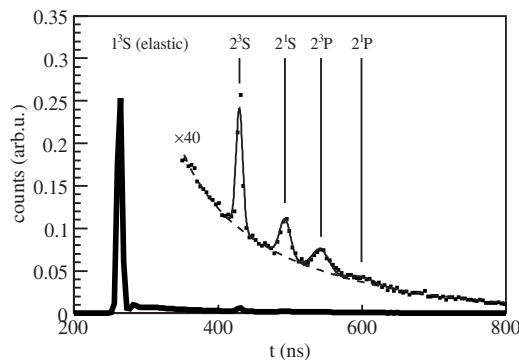


FIG. 2. Time-of-flight spectrum measured at 22 eV, integrated over scattering angles  $\theta=104^\circ-106^\circ$ . Thick line: electron counts as a function of flight time  $t$ , after subtraction of first-order background; symbols: same data (starting at  $t=350$  ns) scaled by 40; thin line: model functions for the fit of the inelastic channels described in the text, shown on top of the model function for the second-order background (thin dashed line); vertical lines: expected ToF values for the four inelastic channels.

with a corresponding increase of DAQ time and experimental error. However, in several measurements of this type we have found an energy spread of the pulsed beam in the range of 80–140 meV (FWHM), which agrees well with the values obtained from ToF spectra (see below). This is a first indication that the pulsing process still has some detrimental effects on the energy distribution of the continuous beam coming from the monochromator. More precise values for the energy spread of the pulsed beam are obtained from the measurement of the helium DCS, and will be discussed in the next section.

## V. DCS MEASUREMENT ON HELIUM

The performance and precision of the spectrometer was tested in a measurement of the angular differential cross section for electron-impact excitation of ground-state helium atoms. A monochromator pass energy of 5 eV was used, yielding a stable electron current of 15–25 nA at the beam crossing, with the pulsing unit switched off. The pass energy of the pulsing unit was set to 10 eV, which fixes the base length of the triangular pulsing voltage to 16 ns, while the amplitude of the pulsing voltage was set to 1.2 V and the pulse repetition rate to 500 kHz. With the pulsing unit on, the current decreased in proportion to the pulsing duty cycle as would be expected. Measurements were performed over the full range of angles accessible.

Figure 2 shows a representative angle slice obtained for the helium target at an electron beam energy of 22 eV, integrated over scattering angles of  $104^\circ-106^\circ$  as explained above (indicated by the thick solid line in the main graph and the dots in the magnified insert). The prominent peak at ToF around 264 ns is caused by electrons which are elastically scattered by the helium target beam. To the left of this peak, the lack of spurious events (unrelated to the timing of the pulsing unit) demonstrates that the electron beam delivered from the pulsed gun has virtually no direct current component. The four smaller peaks at 425, 483, 527, and 575 ns correspond to electron-impact excitation of the  $2^3S$ ,  $2^1S$ ,  $2^3P$ , and  $2^1P$  states of helium, which leaves the scattered electrons with energies of 2.18, 1.38, 1.04, and 0.78 eV, respec-

tively. As can be seen in the figure, the measured positions of all four inelastic channels agree well with the ToF calculated from the known drift distance  $L$  and the scattered electron energies, when the delay occurring in the time measurement (see above) is taken into account. The latter is determined from the difference between the measured position of the elastic peak and the expected flight time of 75 ns for 22 eV electrons.

The elastic peak is of approximately Gaussian shape and has a standard deviation of 4.2 ns. Because of the comparatively high energy of the elastically scattered electrons, almost no ToF broadening from the energy spread of the electron beam is expected for this channel. While the ToF broadening caused by the small difference in drift length between electrons detected at the center of the MCP and those detected at its fringe contributes less than 0.05 ns to the above standard deviation, contributions from the finite extent of the interaction volume are even smaller for this kinematics. Hence, the width of the elastic peak is a good measure of the initial temporal spread  $\sigma_t$  (standard deviation) of the electron pulses produced by the gun. The measured value corresponds to a FWHM of 9.9 ns, which is sufficient for the desired resolution of the ToF spectra (see above).

Although the background of electrons scattered from spectrometer parts or by the residual gas has already been subtracted as described above, a smooth residual background underlying the inelastic peaks can still be seen, which diminishes toward longer ToF. It most likely arises from electrons falling onto the detector after being sequentially scattered by both spectrometer parts and the target beam and is consequently labeled “second order” background, to distinguish it against the “first order” background from single scattering by either residual gas or spectrometer parts alone. This interpretation is backed up by the observation that the intensity of this background seems to follow variations in the magnitude of the elastic peak, regardless of whether these originate from changes in the electron current, the target beam density or the elastic DCS itself. Although the introduction of the semicircular Faraday trap around the target region reduced the second-order background by a factor of at least 2, to the intensity shown in the figure, it was not possible to eliminate it entirely. By its nature, this background cannot be separately measured and then subtracted from the data, as is done with the first-order background. It is therefore subtracted by mathematical methods in the data analysis as described below, using the ROOT software suite<sup>13</sup> provided by CERN.

While the number  $N_{el}$  of elastically scattered electrons is readily obtained by numerically integrating the counts in the elastic peak, the counts  $N_i$  in each inelastic scattering peak  $i$  are separated from the second-order background in a least-squares fit of a model function to all ToF spectra measured at different scattering angles. This function consists of a sum of two exponential functions modeling the shape of the second order background, on which one Gaussian curve is superimposed for every energetically open, inelastic scattering channel of helium. These channel functions are indicated separately, on top of the background, by the thin solid lines in the magnified insert in Fig. 2. To improve the stability of the fit procedure against the selection of the initial guess made for

the free parameters, as well as to reduce the systematical errors of the results, excess free parameters have been eliminated in the model function using known information about the scattered electrons: First, the mean ToF of each Gaussian representing an inelastic channel is calculated from the known beam energy and energy losses, as the flight time required to travel over the length  $L$  between target and detector, plus the delay calculated above from the elastic peak. To account for a possible difference in work function between the drift cone and the target cage, a small ( $\leq 0.2$  eV) shift of the energy scale (equal for all inelastic channels) is allowed as a new free parameter (note that this shift is not an indication of imprecise energy calibration of the primary beam, since the latter is always determined from an *in situ* measurement of the excitation function, as described above).

The total width  $\sigma_i$  of each channel in the ToF spectrum is calculated from the scattered electron energy and the standard deviations  $\sigma_t$  and  $\sigma_E$  of the time and energy distributions of the primary electron pulses. While  $\sigma_t$  was obtained independently from the elastic peak,  $\sigma_E$  must be determined as a free parameter in preliminary fits of the inelastic peaks, which are performed separately for each angle slice. By averaging over all of these preliminary fits, an energy spread of  $\sigma_E = 60 \pm 10$  meV of the pulsed beam was found, corresponding to a FWHM of  $150 \pm 25$  meV. This result was held fixed in a second pass of the fit algorithm, from which the  $N_i$  were finally determined. Therefore, for every angle slice a total of only five free parameters (including the  $N_i$ ) are necessary for the mathematical modeling of all four inelastic channels, plus four additional parameters per slice for the background.

The quality with which the measured spectra are reproduced by the model function is comparable to that demonstrated in Fig. 2, for all  $\theta$ . Analysis of the error correlation matrix between the fit parameters shows that the reproduction of the background is the most important contribution to the systematical error in the obtained  $N_i$ . For very small differential cross sections and long ToF (strong broadening by energy spread), as is the case for the  $2^1P$  channel, this error can reach up to 50%, which far exceeds the contribution from statistical fluctuations. The total error of each  $N_i$  (from both statistics and imperfect modeling) is therefore extracted from the numerical fit procedure, and is included in the individual error bars given on each experimentally obtained cross section. However, because the angular acceptance, transmission, and detection efficiency of our detector are essentially independent of the energy of the electrons, no corrections for these apparatus functions have to be applied to the measured DCS. Also, the scattering volume does not enter the calculation. An absolute differential cross section  $DCS_i(\theta)$  can therefore be determined for each inelastic channel  $i$  by

$$DCS_i(\theta) = \frac{N_i(\theta)}{N_{el}(\theta)} DCS_{el}(\theta), \quad (3)$$

where the DCS of the elastic channel  $DCS_{el}(\theta)$  is usually well known from both theory and previous experiments. Because one of the primary objectives of our measurement was to eliminate the apparatus functions which usually affect the

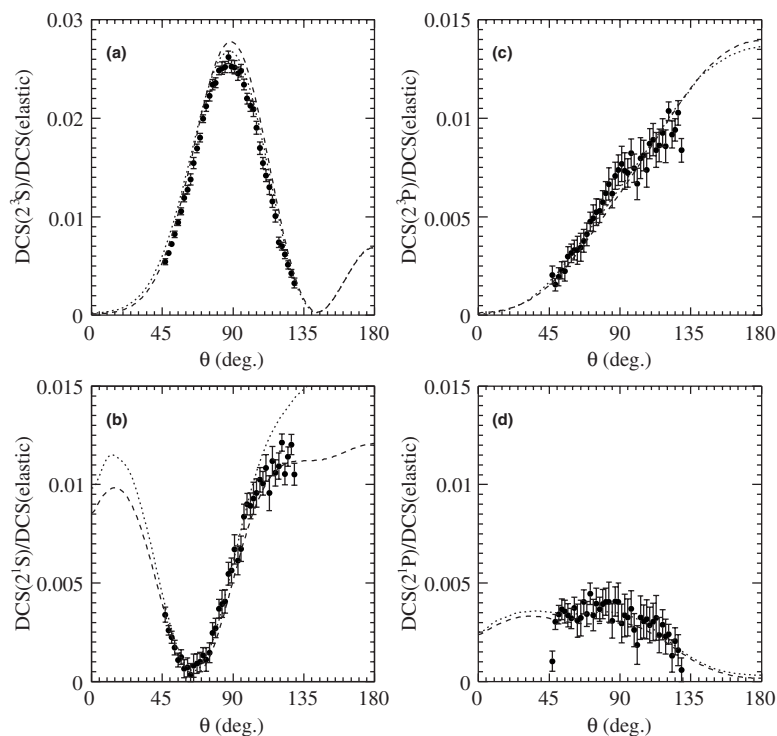


FIG. 3. Angular differential cross sections (DCS) of electron-impact excitation of He at 22 eV beam energy, to (a) the  $2^3S$  state, (b) the  $2^1S$  state, (c) the  $2^3P$  state and (d) the  $2^1P$  state, all relative to the DCS of the elastic channel. Symbols: experimental data; dashed line: CCC calculation;<sup>14</sup> dotted line: *B*-spline *R*-matrix calculation.<sup>15</sup>

outcome of DCS measurements, a comparison of the DCS ratio between the elastic and inelastic channels with theory is of more interest here than their absolute values.

Figure 3 therefore shows the relative cross sections  $DCS_i/DCS_{el}$  measured in this experiment as a function of  $\theta$ , along with two independent calculations, for electron-impact excitation of the four fine structure levels of helium belonging to the principal quantum number  $n=2$ . The individual error bars shown with the data have been obtained from the fit procedure as described above, and include statistical fluctuations as well as imperfections in the modeling of the second-order background. The error bars do not include any experimental error on the overall scale of the relative DCS, which mostly arises from the subtraction of the first-order background, and hence is largely independent of the scattering angle. However, the presence of any second-order background in the elastic channel must be eliminated, since this would systematically shift the measured relative DCS. This is done by observing that even the shortest possible pathway by which electrons could reach the detector, after being scattered elastically by both target beam and a metal surface (i.e., the target enclosure) in sequence, already leads to a ToF which is 10 ns longer than that for the direct path associated with the actual elastic scattering signal. With this information, the elastic second-order background may actually be identified in Fig. 2, as the small peak immediately following the elastic one. It is readily discriminated against by choosing proper limits for integrating over the elastic peak, so that the second order background contribution to the number of elastic events can safely be considered negligible.

Figure 3(a) shows the relative DCS obtained for the  $2^3S$  channel. In this case, the experimental error bars are very small, partly because of the large cross section for this channel, but also because the energy of the scattered electrons is comparatively high (2.18 eV). This reduces the width of the

inelastic peak in the ToF spectrum and hence the influence of the second-order background on the result. Another consequence of the high scattered energy is that the experimental error in the overall scale of the relative DCS is estimated to be only 5%–10% of the respective DCS value (see below for discussion).

The individual error bars for the  $2^1S$  and  $2^3P$  channels in Figs. 3(b) and 3(c) are somewhat larger than for the  $2^3S$  channel, but we believe the scale error to be comparable because of the relatively large energy of the scattered electrons.

The situation is different for the  $2^1P$  channel shown in Fig. 3(d), where a small cross section and strong ToF broadening make the separation of signal and second-order background more difficult. The total error extracted from the fit is mainly related to the quality with which the second-order background can be represented, and varies between 30% and 50% of the relative DCS, depending on the magnitude of the latter. The scaling error of the DCS axis is also expected to be somewhat larger for this channel: as the kinetic energy of the scattered electrons is only a fraction of an electron volt, transmission to the detector is more likely to be affected by variations in surface potential (possibly caused by adsorbates on the copper mesh terminating the field-free region) and by the presence of magnetic fields up to 1  $\mu$ T near the detector, which cannot be fully shielded or compensated. We therefore estimate the total scale error of the relative DCS to be  $\pm 10\%$  for scattered electron energies above 1 eV, and  $\pm 15\%$  for energies below this value.

For comparison with our measurements, Fig. 3 also shows the results of two recent theoretical calculations. The dashed line represents a convergent close-coupling (CCC) calculation by Fursa and Bray which, aside from improvements in the description of the target and the number of coupled states, has been described in Ref. 14. The other cal-

ulation, indicated by the dotted line in Fig. 3 shows the results of Zatsarinny *et al.*,<sup>15–17</sup> who used a B-spline  $R$ -matrix approach. Overall, the agreement between our experiment and both theories is exceptionally good, even in the case of the very weak  $2^1P$  channel, with the respective differences being smaller or comparable to the experimental scale errors established above. Only for the  $2^1S$  channel and at large scattering angles an appreciable difference can be seen between the two calculations, with the experimental results being marginally in favor of the CCC curve. However, since a more detailed discussion of the differences between experiment and theory, as well as a comparison between the different theoretical techniques is beyond the scope of this paper, we refer the reader to Ref. 18.

## VI. CONCLUSIONS AND OUTLOOK

We have built a novel ToF electron spectrometer working with a pulsed electron beam which exhibits an energy spread approximately four times smaller than that achieved by previous comparable apparatuses. The ToF method together with the field-free drift of the electrons after the scattering relieves us of the need for complicated and cumbersome calibrations of the beam overlap volume and the apparatus transmission function, which is commonly associated with using electrostatic energy analyzers in the detection branch of a spectrometer.

The energy width of the beam produced by the pulsed electron gun was deduced to be 150 meV from the ToF broadening of the inelastic signals in the spectra measured for helium. This is still larger by a factor of 2–3 compared to the unpulsed but monochromatized beam, which indicates that some aspects of the influence of the pulsing scheme on the beam energy distribution are still unclear. One possible candidate is the presence of ringing and signal distortions on the cables transmitting the pulsing transients to the deflector plates of the pulsing unit. Deviations from the ideal triangular signal shape have been observed to be present to a small degree (approximately 10% of the transient amplitude) but no straightforward way could be found to reduce them. Since the two transients are affected differently (by sign and amplitude), the requirement that the electric potential at the middle plane of the deflector gap be constant in time is not fulfilled exactly and may lead to energy broadening of the pulsed beam.

However, energy resolution was not critical for the quality of the presented measurement. Instead, the error bar of the obtained differential scattering cross sections is determined by the presence of a background of inelastic scattering events in the ToF spectra, which cannot be suppressed or

subtracted entirely. Given that this experiment took place at scattered energies of an electron volt or less for some of the inelastic channels, the measured cross section is of very good quality, and withstands comparison to several state-of-the-art theoretical calculations.

The spectrometer itself will, in the future, be used to investigate the threshold behavior of electron-impact excitation of various atomic and molecular targets. In particular, at the time of this writing an experiment on nitrogen molecules is being conducted, where the DCS is measured at energies above 10 eV, which is close to the thresholds of low-lying electronically excited states. In this region, there has been a long-standing debate about the absolute magnitude of the DCS,<sup>1</sup> which has been found to vary between different experiments by up to a factor of 5. Since our technique is complementary to that employed in most other experiments, we hope to contribute toward the clarification of this issue.

## ACKNOWLEDGMENTS

The authors would like to thank the staff of the Atomic and Molecular Physics Laboratories mechanical workshop for their continuous support. M.L. would also like to thank both the Australian Research Council and the Deutsche Forschungsgemeinschaft, who have supported the project under Grant Nos. LX0346836 and LA 1473, respectively.

<sup>1</sup>M. J. Brunger and S. J. Buckman, *Phys. Rep.* **357**, 215 (2002).

<sup>2</sup>M. Allan, *J. Phys. B* **38**, 3655 (2005).

<sup>3</sup>M. A. Khakoo, P. V. Johnson, I. Ozkay, P. Yan, S. Trajmar and I. Kanik, *Phys. Rev. A* **71**, 062703 (2005).

<sup>4</sup>J. R. LeClair, S. Trajmar, M. A. Khakoo, and J. C. Nickel, *Rev. Sci. Instrum.* **67**, 1753 (1996).

<sup>5</sup>C. Ma, P. B. Liescheski, and R. A. Bonham, *Rev. Sci. Instrum.* **60**, 3661 (1989).

<sup>6</sup>S. N. Samarin, O. M. Artamonov, D. K. Waterhouse, J. Kirschner, A. Morozov, and J. F. Williams, *Rev. Sci. Instrum.* **74**, 1274 (2003).

<sup>7</sup>M. Lange, J. Matsumoto, A. Setiawan, J. C. A. Lower, and S. J. Buckman, *J. Electron Spectrosc. Relat. Phenom.* **144–147**, 993 (2005).

<sup>8</sup>J. R. Pierce, *J. Appl. Phys.* **11**, 548 (1940).

<sup>9</sup>J. M. B. Bakker, *J. Phys. E* **6**, 785 (1973).

<sup>10</sup>D. A. Dahl, *Int. J. Mass. Spectrom.* **200**, 3 (2000).

<sup>11</sup>O. Jagutzki, V. Mergel, K. Ullmann-Pfleger, L. Spielberger, U. Spillmann, R. Dörner, and H. Schmidt-Böcking, *Nucl. Instrum. Methods Phys. Res. A* **477**, 244 (2002).

<sup>12</sup>S. J. Buckman, P. Hammond, F. H. Read, and G. C. King, *J. Phys. B* **16**, 4039 (1983).

<sup>13</sup>R. Brun and F. Rademakers, *Nucl. Instrum. Methods Phys. Res. A* **389**, 81 (1997).

<sup>14</sup>D. V. Fursa and I. Bray, *Phys. Rev. A* **52**, 1279 (1995).

<sup>15</sup>O. Zatsarinny, *Comput. Phys. Commun.* **174**, 273 (2006).

<sup>16</sup>O. Zatsarinny and K. Bartschat, *J. Phys. B* **37**, 2173 (2004).

<sup>17</sup>O. Zatsarinny and C. Froese Fischer, *J. Phys. B* **33**, 313 (2000).

<sup>18</sup>M. Lange, J. Matsumoto, J. C. A. Lower, S. J. Buckman, O. Zatsarinny, K. Bartschat, I. Bray, and D. Fursa, *J. Phys. B* **39**, 4179 (2006).